Effect of platinum substitution on the structural and magnetic properties of Ni$_2$MnGa ferromagnetic shape memory alloy

Sanjay Singh,[1,*] S. W. D'Souza,[1] J. Nayak,[1] L. Caron,[1] E. Suard,[2] S. Chadov,[1] and C. Felser[1]

[1]*Max Planck Institute for Chemical Physics of Solids, Nöthnitzer Str. 40, D-01187 Dresden, Germany*
[2]*Institut Laue-Langevin, Boîte Postale 156, 38042 Grenoble Cedex 9, France*

Ni$_2$MnGa exhibits ideal ferromagnetic shape memory properties, however, brittleness and a low-temperature martensite transition hinder its technological applications motivating the search for novel materials showing better mechanical properties as well as higher transition temperatures. In this work, the crystal structure, phase transitions, and the magnetic properties of quaternary Ni$_{2-x}$Pt$_x$MnGa ($0 \leqslant x \leqslant 1$) shape memory alloys were studied experimentally by x-ray diffraction, magnetization measurements, and neutron diffraction and compared to *ab initio* calculations. Compositions within $0 \leqslant x \leqslant 0.25$ exhibit the cubic austenite phase at room temperature. The $x \approx 0.3$ composition exhibits a seven-layer modulated monoclinic martensite structure. Within $0.4 \leqslant x \leqslant 1$, the system stabilizes in the nonmodulated tetragonal structure. The martensite transition has very narrow thermal hysteresis $0 \leqslant x \leqslant 0.3$, which is a typical characteristic of a shape memory alloy. By increasing x, the temperature of the martensite transition increases, while that of the magnetic transition decreases. The $x = 1$ composition (NiPtMnGa) in the martensite phase undergoes a para-to-ferrimagnetic transition. The saturation magnetization exhibits a nontrivial behavior with increasing up to $x \approx 0.25$, above which, it suddenly decreases. Powder neutron diffraction reveals the presence of antisite disorder, with about 17% of the original Ga sites being occupied by Mn. Computations suggest that the antisite disorder triggers an antiferromagnetic coupling between two Mn atoms in different crystallographic positions, resulting into a sudden drop of the saturation magnetization for higher x.

I. INTRODUCTION

Ferromagnetic shape memory alloys (FSMAs) have gained broad interest in recent years due to a large magnetic field induced strain (MFIS) [1–3], which suggests their efficient use in magnetic actuators. The large MFIS in these systems is related to the shape change upon an external magnetic field applied onto the low-temperature martensite phase. The martensite transition represents a diffusionless phase transformation in which a material undergoes a structural transition from a high-symmetry cubic austenite phase into a lower-symmetry martensite phase by shear deformation [4]. The martensite phase contains twinned variants coupled with their magnetic moments. Application of an external magnetic field triggers the simultaneous movement of the twinned variants acting on their magnetic moments coupled to the structure via the large magnetocrystalline anisotropy. This induces a huge but recoverable deformation in the material.

Among different FSMAs, the Ni$_2$MnGa Heusler alloy is the most studied system. It exhibits martensite and ferromagnetic transitions at 202 and 373 K, respectively [5]. In addition to the large MFIS ($\sim$10%), it also shows other multifunctional properties, such as large negative magnetoresistance [6–8] and magnetocaloric effect [9–11], which have straightforward technological implementations. Another effect observed in Ni$_2$MnGa, strongly enhancing its importance in basic physical aspects, is the formation of the premartensite phase and the accompanying charge density wave [12,13]. However, the brittleness and low transition temperatures of Ni$_2$MnGa motivate the search for systems with better mechanical

properties as well as higher transition temperatures [8,14,15]. To obtain new FSMAs replacing Ni$_2$MnGa, huge efforts have been made [16–21]. Recent *ab initio* studies predicted that Pt-doped Ni$_2$MnGa can be an alternative to Ni$_2$MnGa [22]. In particular, Pt substitution on the Ni site generates a series of magnetic shape-memory alloys with properties similar to Ni-Mn-Ga, but with a larger strain (of 14%) [22–24]. This agrees well with experimental studies on 10% Pt-doped Ni-Mn-Ga showing that it has a higher martensite transition temperature (285 K) compared to Ni$_2$MnGa (210 K) [25,26]. The powder neutron diffraction study of the martensite phase reveals its 7M-modulated orthorhombic structure, similar to that of Ni$_2$MnGa, indicating that it is likely to exhibit magnetic field induced strain. At the same time, the volume difference between the austenite and the martensite phases is less than 0.5%, as it would be expected for a volume-conserving martensite transformation [26]. In addition, the martensite phase of Ni$_{1.8}$Pt$_{0.2}$MnGa reveals a signature of a large magnetocrystalline anisotropy, supported by the change from inverse-to-direct magnetocaloric effect at 1.6 T [27]. Thus the theoretical results supported by the initial experimental study on a 10% Pt-doped Ni-Mn-Ga indicate that the quaternary Ni$_{2-x}$Pt$_x$MnGa FMSA-s are good candidates for large MFIS. However, a detailed investigation of structural and magnetic properties of Pt-doped Ni$_2$MnGa with varying Ni-Pt concentration is necessary to understand the Ni-Pt-Mn-Ga system, which will help to use these alloys for future applications as magnetic actuators.

Here, we studied the structural and magnetic properties of Ni$_{2-x}$Pt$_x$MnGa ($0 \leqslant x \leqslant 1$) alloys using x-ray diffraction, magnetization, and neutron diffraction measurements. Additional *ab initio* calculations have been done for better understanding of the composition-dependent saturation

---
*sanjay.singh@cpfs.mpg.de

magnetization behavior. By increasing the Pt content x in $Ni_{2-x}Pt_xMnGa$ the martensite transition temperature is found to increase, whereas the magnetic transition temperature decreases. However, the saturation magnetization shows unusual behavior in contrast to the earlier theoretical studies [22,23]. The saturation magnetization initially increased up to $x \approx 0.25$ and is then reduced with further increasing x. These theoretical results as well as the results of neutron diffraction reveal the increasing antiferromagnetic interactions due to antisite disorder with increasing Pt content in $Ni_{2-x}Pt_xMnGa$.

II. EXPERIMENTAL AND THEORETICAL DETAILS

Polycrystalline ingots of $Ni_{2-x}Pt_xMnGa$ ($0 \leqslant x \leqslant 1$) have been prepared by melting appropriate quantities of Ni, Pt, Mn, and Ga of 99.99% purity in an arc furnace. Ingots were then annealed at 1100 K ($0 \leqslant x \leqslant 0.15$), 1173 K ($x = 0.25$ and 0.3), and at 1273 K ($x = 0.4, 0.5, 0.7$, and 1) for 3 days to obtain homogeneity and subsequently quenched into ice water. The structural characterization was performed at room temperature (RT) with powder x-ray diffraction (XRD) using Cu K_α radiation. The magnetic properties and transition temperatures were measured using a SQUID-VSM magnetometer. Neutron diffraction measurements were performed at the D2B high-resolution neutron powder diffractometer (ILL, Grenoble). A vanadium cylinder was used as a sample holder. The data were collected at 300 K using a neutron wavelength of 1.59 Å in the high-intensity mode. The analysis of diffraction patterns were done with JAVA2006 and FULLPROF software packages [28].

Ab initio calculations have been carried out using the spin-polarized relativistic Korringa-Kohn-Rostocker method (SPRKKR) [29]. The substitutional disorder as well as the antisite disorder in $Ni_{2-x}Pt_xMnGa$ ($0 \leqslant x \leqslant 1$) were accounted for by the coherent potential approximation (CPA) [30,31]. The exchange-correlation was treated by the standard local density approximation (LDA) [32]. Brillouin zone integration was performed on a $18 \times 18 \times 18$ k mesh. The angular momentum expansion holds up to $l_{max} = 3$ (d symmetry). The energy convergence criterion and the CPA tolerance has been set to 10^{-5} Ry.

III. RESULTS AND DISCUSSION

A. Room-temperature crystal structure of $Ni_{2-x}Pt_xMnGa$ ($0 \leqslant x \leqslant 1$)

Typical Heusler alloys of X_2YZ composition (with X and Y being transition elements and Z is a main group element) exhibit cubic $L2_1$ crystal structure (austenite phase) with Fm$\bar{3}$m space group (SG) symmetry. X atoms occupy the $8c$ Wyckoff sites, (0.25, 0.25, 0.25) and (0.75, 0.75, 0.75), while the Y and Z atoms occupy the $4a$ (0, 0, 0) and $4b$ (0.5, 0.5, 0.5) sites, respectively. In the martensite phase these Heusler alloys may show a tetragonal structure, which corresponds to SG $I4/mmm$. This structure has three Wyckoff sites, $4d$ (0, 0.5, 0.25), $2a$ (0, 0, 0) and $2b$ (0, 0, 0.5) occupied by X, Y, and Z elements, respectively. Both structures with indication of their Wyckoff positions are shown in Fig. 1. Some Heusler alloys crystallize in more complicated martensite structures, which are modulated. The Ni-Mn-Ga family of Heusler alloys is a typical example, which shows the cubic
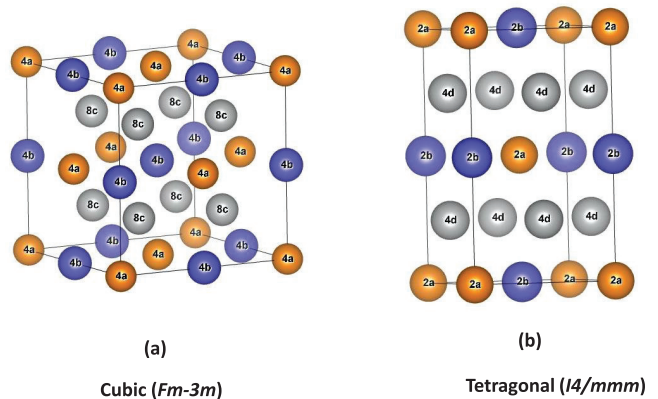

FIG. 1. Crystal structure of (a) cubic (austenite) and (b) tetragonal (martensite) phase. Wyckoff positions are indicated within the unit cells.

$L2_1$ structure in the austenite phase and in the martensite phase they exhibit tetragonal [5], orthorhombic 3M- (premartensite), and 7M- (martensite) modulations [3,12]. The temperature and compositional dependent change in the martensite structures, the sequence of their occurrence and their stability has been widely studied in the Ni-Mn-Ga Heusler alloys from both experiment [33–37] and theory [38–41].

1. Structure in the composition range of $0 \leqslant x \leqslant 0.25$

The Rietveld refinements of RT XRD patterns for $Ni_{2-x}Pt_xMnGa$ ($0 \leqslant x \leqslant 0.25$) are shown in Fig. 2. For all samples the Bragg reflections were indexed well by the cubic $L2_1$ structure (SG Fm$\bar{3}$m), which follows from the small difference between observed and calculated XRD patterns. For the stoichiometric Ni_2MnGa case ($x = 0$), Ni occupies the $8c$ sites of the cubic $L2_1$ cell, while $4a$ and $4b$ are occupied by Mn and Ga, respectively. In $Ni_{2-x}Pt_xMnGa$, Pt atoms randomly share $8c$ positions with Ni. The lattice parameter obtained from the refinement for Ni_2MnGa is $a = 5.82243(9)$ Å, which is in good agreement with literature [42,43]. Increasing Pt content, a increases: for $Ni_{1.75}Pt_{0.25}MnGa$ ($x = 0.25$) it reaches 5.87609(2) Å.

2. 7M-modulated martensite structure at $x = 0.3$

The XRD pattern (Fig. 3) of the $x = 0.3$ sample is more complicated compared to the compositions with lower Pt content. It indicates that at RT the sample is not in the austenite phase, which is also confirmed by the low-field magnetization measurement showing the martensite transition at 320 K that is well above RT (see Fig. 7).

In general, the system undergoes a transition from cubic austenite to $L1_0$ type tetragonal structure resulting from the lattice deformation strain of the cubic austenite phase. The splitting of the (2 2 0) and (4 0 0) Bragg reflections of the cubic $L2_1$ phase into doublets is generally observed for a tetragonal martensite, which belongs to the SG $I4/mmm$ [43,44]. However, in the present case there are more than two reflections observed in the vicinity of the most intense peak (220) of $L2_1$ phase, which clearly disfavors the tetragonal distortion of the structure in the martensite phase. We have also ruled out the possibility of coexistence of cubic $L2_1$ and
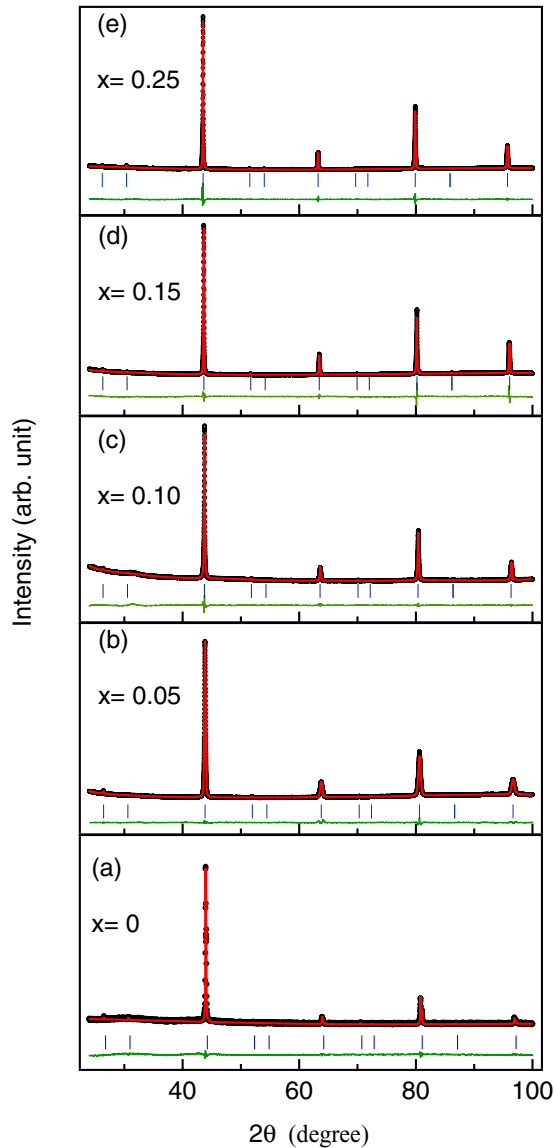
FIG. 2. Rietveld refinements of RT XRD patterns for $Ni_{2-x}Pt_xMnGa$ ($0 \leqslant x \leqslant 0.25$). The experimental data, fitted curve, and the residue are shown by dots (black), continuous line (red), and bottom-most plot (green), respectively. The tick marks (blue) represent the Bragg peak positions.

FIG. 3. LeBail refinements of the RT XRD pattern of $Ni_{1.7}Pt_{0.3}MnGa$ ($x = 0.3$) by considering (a) a combination of the cubic and tetragonal, (b) 7M-modulated orthorhombic, and (c) Rietveld refinements with 7M-modulated monoclinic unit cells. The experimental data, fitted curve, and the residue are shown by dots (black), continuous line (red), and bottom-most plot (green), respectively. The tick marks (blue) represent the Bragg peak positions. The inset shows main peak region in an expanded scale. Arrows (blue) indicates Bragg reflections, which were not indexed with the assumed model in the refinement.

tetragonal $L1_0$ phases by considering a two phase model using the LeBail refinement procedure, which was unable to index some of the Bragg reflections indicated by blue arrows in Fig. 3(a).

This type of complex XRD patterns of FSMAs are reported in literature and are generally related to the structural modulation of the low-temperature martensite phase and assigned as the modulated form of the lower-symmetry orthorhombic or monoclinic unit cell [26,42,43,45–48]. The powder neutron diffraction study of the low-temperature martensite phase of $Ni_{1.8}Pt_{0.2}MnGa$ shows that it has 7M-modulation (SG *Pnnm*), which is similar to the martensite structure of Ni_2MnGa [26]. Therefore, to investigate the RT crystal structure of $Ni_{1.7}Pt_{0.3}MnGa$, we initially carried out the LeBail refinement using the 7M-modulated orthorhombic structure, which did

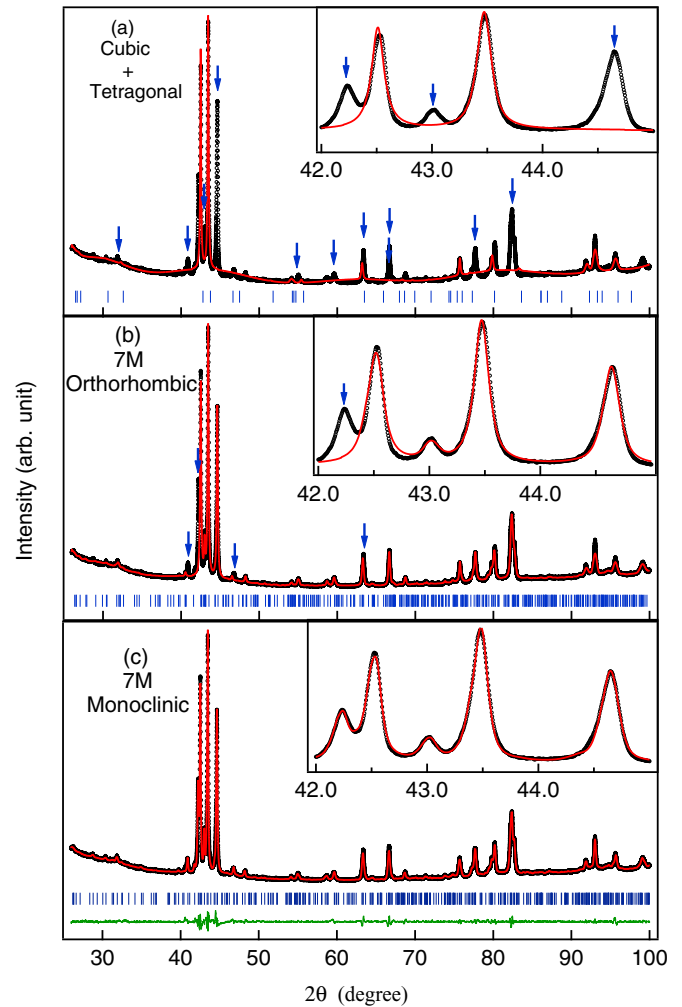not account for some of the peaks satisfactorily [indicated by blue arrows in Fig. 3(b)]. All Bragg reflections could only be accounted for considering a monoclinic structure with lattice parameters $a = 4.279$ Å, $b = 5.606$ Å, $c = 29.756$ Å, and $\beta = 93.009°$ within SG $I2/m$. Here, $c \approx 7 \times a$ indicates a 7M modulation. Similar structures with modulated monoclinic or orthorhombic symmetry have been reported for Ni-Mn-Ga [45,46,49,50]. For those structures, which exhibit modulation in Ni-Mn-Ga alloys, a large strain induced by magnetic field has been observed [2].

After obtaining the unit cell parameters and the space group (SG $I2/m$) of the 7M-modulated structure from the LeBail refinement, we have performed the Rietveld analysis considering all atomic positions. We find that the 7M-modulated structure of $Ni_{1.7}Pt_{0.3}MnGa$ consists of 12 different
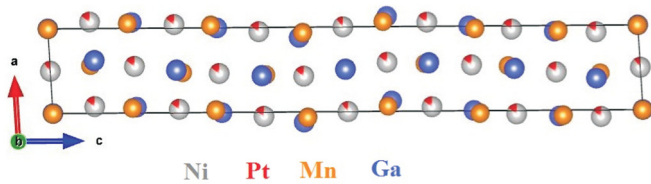
FIG. 4. The 7M-modulated monoclinic unit cell of $Ni_{1.7}Pt_{0.3}MnGa$ martensite phase projected onto the *ac* plane.

crystallographic positions within the monoclinic unit cell. Four of these positions are occupied by Mn, four by Ga and four by Ni and Pt together according to their relative occupancies. The Mn1 occupies the 2*a* (0, 0, 0) position. Mn2, Mn3, and Mn4 occupy position 4*i* (*x*, 0, *z*), where the *z* coordinate equals to 1/7, 2/7, and 3/7 according to the 7M modulation, respectively, whereas the *x* coordinate was refined. Ga1 occupies the 2*b* (0, 0.5, 0) position, Ga2, Ga3, and Ga4 the 4*i* (*x*, 0, *z*). Ni1/Pt1 randomly occupy 4*h* (0.5, *y*, 0); Ni2/Pt2, Ni3/Pt3, and Ni4/Pt the 8*j* (*x*, 1/4, *z*). Figure 3(c) shows the experimental and calculated patterns, as well as their difference, obtained from the Rietveld refinement. The inset of Fig. 3(c) depicts the fit within the 42°–45° range of 2*θ*. The excellent match between the observed and the calculated peak profiles suggests that our structural model is correct and $Ni_{1.7}Pt_{0.3}MnGa$ has a 7M-modulated martensite phase at RT with monoclinic symmetry of SG $I2/m$. The refined structural parameters are given in Table I. The modulation waves for different atoms (Ni/Pt, Mn, and Ga) are clearly observed in Fig. 4. A larger amplitude of modulation is observed for Mn and Ga than for Ni, which is different compared to the Ni_2MnGa [45,46,48].

3. Structure in the composition range of $0.4 \leqslant x \leqslant 1$

For higher Pt doped Ni-Mn-Ga samples (*x* = 0.4, 0.5, 0.7, and 1) the XRD patterns at RT are shown in Fig. 5. The

TABLE I. Lattice parameters, space group, and atomic positions (x, y, z) of $Ni_{1.7}Pt_{0.3}MnGa$ in the martensite phase at RT.

Crystal system	Monoclinic		
SG	$I2/m$		
Cell (Å)	$a = 4.2797(6)$, $b = 5.6063(7)$, $c = 29.756(3)$		
	$\beta = 93.0091(1)°$		

Atom	Wyckoff	*x*	*y*	*z*
Mn1	2*a*	0	0	0
Mn2	4*i*	0.060(4)	0	1/7
Mn3	4*i*	0.027(3)	0	2/7
Mn4	4*i*	0.936(4)	0	3/7
Ga1	2*b*	0	0.5	0
Ga2	4*i*	0.071(3)	0.5	1/7
Ga3	4*i*	0.996(3)	0.5	2/7
Ga4	4*i*	0.878(2)	0.5	3/7
0.85Ni1+0.15Pt1	4*h*	0.5	0.25	0
0.85Ni2+0.15Pt2	8*j*	0.5498(19)	0.25	1/7
0.85Ni3+0.15Pt3	8*j*	0.4598(15)	0.25	2/7
0.85Ni4+0.15Pt4	8*j*	0.4207(18)	0.25	3/7
		$\chi^2 = 4.50$		

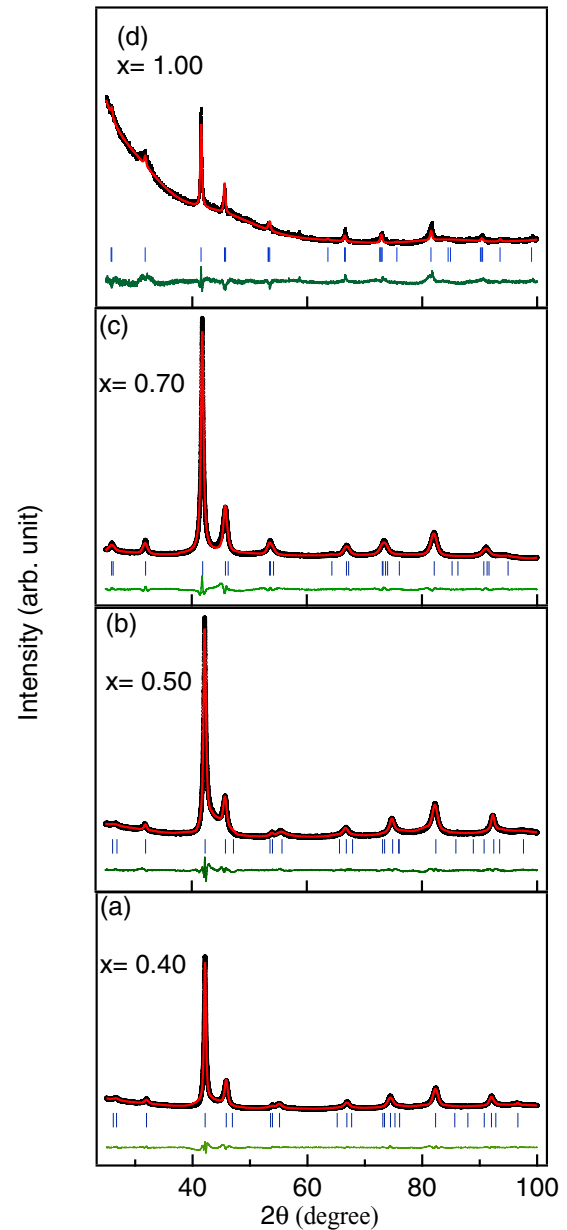
FIG. 5. Rietveld refinements for RT XRD patterns of *x* = 0.4, 0.5, 0.7, and 1. The experimental data, fitted curve, and the residue are shown by dots (black), continuous line (red), and bottom-most plot (green), respectively. The tick marks (blue) represent the Bragg peak positions.

twofold splitting of the (220) Bragg peak of the cubic $L2_1$ structure indicates the stabilization of the tetragonal martensite phase. This tetragonal structure can be fit by the body-centered tetragonal SG $I4/mmm$ with two formula units per unit cell ($Z = 2$) as well as by the face-centered orthorhombic SG $Fmmm$ with $Z = 4$ [5,42,44]. In SG $I4/mmm$, the splitting of the (2 2 0) Bragg peak of the cubic $L2_1$ structure can be indexed with (1 1 2) and (2 0 0), while in SG $Fmmm$ the splitting if the (2 2 0) Bragg peak can be indexed with (2 2 0) and (2 0 2) Bragg reflections. Here we have performed the Rietveld refinement by taking into account SG $I4/mmm$. In this structure, Ni and Pt atoms sit in the 4*d* Wyckoff positions

TABLE II. Lattice constants obtained from the refinement for $Ni_{2-x}Pt_xMnGa$ ($x = 0.4$, 0.5, 0.7, and 1) and at room temperature for body centered tetragonal unit cell (SG $I4/mmm$) and the corresponding values for the face centered tetragonal unit cell (SG $Fmmm$).

Composition (x)	SG $I4/mmm$	SG $Fmmm$
0.4	$a_I = 3.95351(12)$ Å	$a = 5.590$ Å
	$c_I = 6.59801(3)$ Å	$c = 6.598$ Å
0.5	$a_I = 3.95453(12)$ Å	$a = 5.593$ Å
	$c_I = 6.65813(34)$ Å	$c = 6.658$ Å
0.7	$a_I = 3.9532(1)$ Å	$a = 5.5740$ Å
	$c_I = 6.7607(5)$ Å	$c = 6.7607$ Å
1.0	$a_I = 3.97201(13)$ Å	$a = 5.6164$ Å
	$c_I = 6.84310(41)$ Å	$c = 6.8431$ Å

(according to their relative occupancy), while Mn and Ga sit in 2a and 2b, respectively. To account for the anisotropic broadening of the peak in the diffraction pattern, we have also included the strain parameters during refinement. With this structure model we were able to index all Bragg reflections.

The refined lattice parameters a_I, c_I, where subscript I stands for the body centered tetragonal unit cell and the corresponding lattice parameters for the face-centered SG calculated by using $a = a_F = \sqrt{2}a_I$ and $c = c_F = c_I$ are summarized in Table II for $x = 0.4$, 0.5, 0.7, and 1. Thus the c/a ratio turned out to be 1.19 and 1.18, respectively for $x = 0.4$ and 0.5. For $x = 0.7$ ($Ni_{1.3}Pt_{0.7}MnGa$) and $x = 1$ (NiPtMnGa), the lattice constants are $a = 5.5740$ Å, $c = 6.7607$ Å, and $a = 5.6164$ Å, $c = 6.8431$ Å (Table II), which give c/a ratios of 1.21 and 1.22, respectively.

Although the large MFIS is generally expected for modulated martensite structures [2,3], a literally giant MFIS has been obtained recently for a nonmodulated tetragonal martensite in $Ni_{46}Mn_{24}Ga_{22}Co_4Cu_4$ [51]. Sozinov *et al.* relate the observation of huge MFIS with the reduced c/a ratio compared to the nonmodulated tetragonal phase of Ni_2MnGa ($c/a \approx 1.25$). Thus they have concluded that the small twinning stress due to a smaller c/a value might be responsible for the large MFIS [51,52]. The smaller value of c/a (1.18 and 1.19 for $x = 0.4$ and 0.5, respectively) compared to the nonmodulated tetragonal stoichiometric alloy ($c/a \approx 1.25$) indicates the possibility of large MFIS.

4. Composition-dependent lattice parameters and volume change

The compositional dependence of the lattice parameters and volume at room temperature are shown in Fig. 6. The linear variation of a shows that it follows Vegard's law, which is similar to the case of the Ni-Mn-Ga series in which Ni substitutes Mn [42]. For $x = 0.3$ the c/a ratio is less than 1, which is expected for the modulated martensite structure [41]. With further Pt increase ($0.4 \leqslant x \leqslant 1$) the tetragonal phase is stabilised and the variation in c is larger than in a which indicates that with increasing Pt content the c/a ratio increases. As the c/a ratio represents the tetragonal distortion in Heusler alloys, the lattice parameter variation shows that the tetragonal distortion increases linearly with increasing Pt
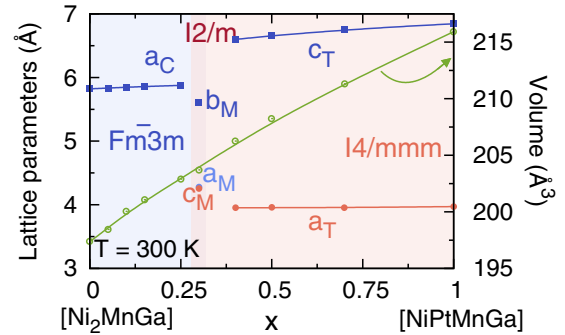

FIG. 6. Lattice parameters and volume at room temperature for $Ni_{2-x}Pt_xMnGa(0 \leqslant x \leqslant 1)$. Subscript "c," "M," and "T" stands for the cubic, monoclinic and tetragonal structures, respectively. Here, $C_M = c/7$, where "c" is the lattice parameter of the 7M-modulated monoclinic unit cell. The corresponding space groups are also indicated. The green circles connected with green lines represent the volume of the unit cell. For comparison with cubic, the volume of the monoclinic and tetragonal unit cells have been multiplied by two.

substitution in $Ni_{2-x}Pt_xMnGa$. It can be also observed from Fig. 6 that the unit cell volume increases almost linearly with increasing Pt, which can be attributed to the difference in the ionic radii of the Ni and Pt atoms.

B. Structural (martensite) and magnetic phase transitions of $Ni_{2-x}Pt_xMnGa(0 \leqslant x \leqslant 1)$

The structural and magnetic transition temperatures as a function of Pt composition have been determined from low-field magnetization measurements ($M(T)$) within $2 < T < 400$ K (Fig. 7). The martensite start ($T_M^s = T_M$), martensite finish (T_M^f), austenite start (T_A^s) and austenite finish (T_A^f) temperatures were obtained from the inflection point on the $M(T)$ curves during cooling (blue) and heating (red), respectively, for composition within $0 \leqslant x \leqslant 0.4$. The sudden drop of $M(T)$ with cooling corresponds to the T_M^s, which is related with the large magnetocrystalline anisotropy of the martensite phase [53]. For stoichiometric Ni_2MnGa ($x = 0$) T_M^s and T_M^f are 211 and 200 K, while T_A^s and T_A^f are 207 and 216 K, respectively. The ferromagnetic (FM)-paramagnetic (PM) transition temperature is $T_C = 373$ K. The premartensite phase transition temperature is observed at $T_P = 259$ K. These transition temperatures agree with the literature [48,53,54]. The compositions $x = 0.05$ and $x = 0.1$ also show the premartensite transition at 250 and 259 K, respectively, similar to the stoichiometric Ni_2MnGa. The compositional dependent structural and magnetic phase diagram the for $Ni_{2-x}Pt_xMnGa$ constructed based on the values obtained from $M(T)$ (Fig. 7) is shown in Fig. 8(a).

The substitution of Ni with Pt in Ni_2MnGa results into an increase of the T_M^s from 211 K ($x = 0$) to 322 K ($x = 0.4$) with $T_M^s < T_C$ Fig. 8(a). For $x = 0.5$ the martensite transition does not occur in the range of temperature of the magnetic phase [Fig. 7(h)]. It is interesting to note that the compositions $x = 0.7$ amd $x = 1$ (NiPtMnGa) exhibit a drop in the $M(T)$ below RT (at $\sim$299 and $\sim$290 K), similar to the austenite-to-martensite transition observed in the samples with lower Pt concentrations. This finding is in contrast with the XRD
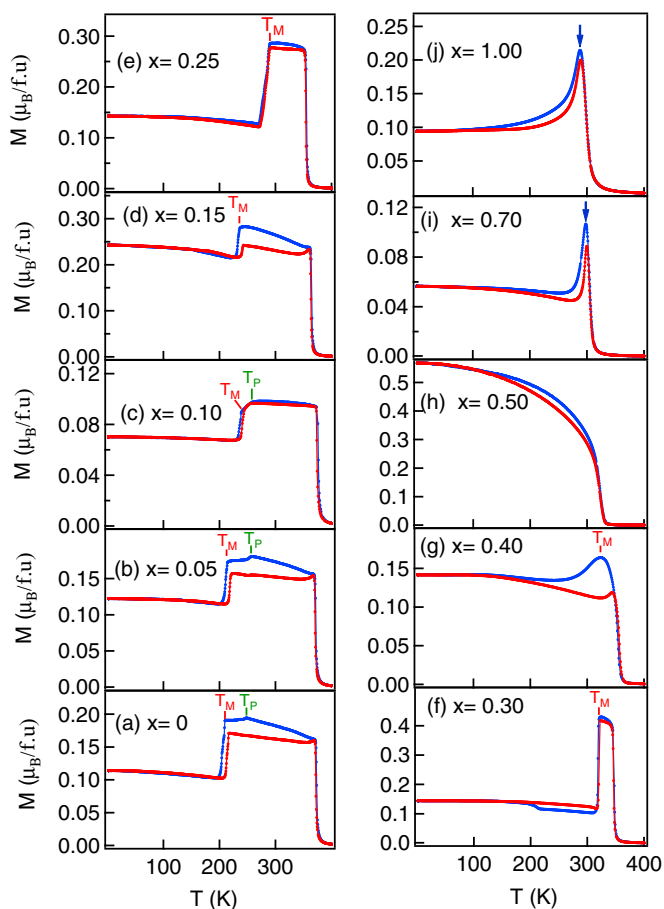
FIG. 7. Low-field (100 Oe, 500 Oe for $x = 1$) magnetization curves (red during heating and blue during cooling) for $Ni_{2-x}Pt_xMnGa$ ($0 \leqslant x \leqslant 1$) exhibiting structural and magnetic transitions. T_M ($=T_M^s$) and T_P are the martensite starting and the premartensite transition temperatures, respectively. Blue arrow show the magnetic transition within the martensite phase.

results, which clearly show the martensite (tetragonal) phase at RT. Although, the stress-induced martensite phase has been reported earlier for some of the Heusler alloys with excess Mn content [50,55–57], the XRD pattern of NiPtMnGa presented in Fig. 5(d) has been recorded on the powder sample, which was further annealed after grinding. This avoids the possibility
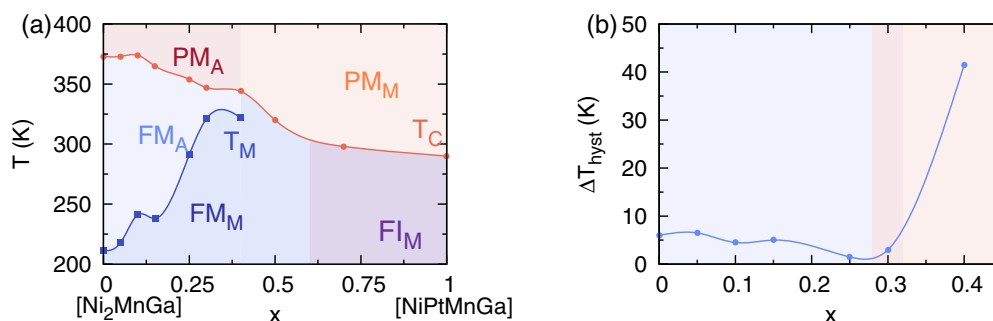
of residual stress which may stabilize the martensite phase above T_M^s [57]. This indicates that this may be a transition from paramagnetic to ferrimagnetic (FI) states occurring completely within the martensite phase, which has been also observed in other Heusler alloys [58].

The width of the thermal hysteresis of the martensite transformation is a critical characteristic of the shape memory behavior. We estimate it as $\Delta T_{hyst} = (T_M^s + T_M^f)/2 - (T_A^s + T_A^f)/2$ as shown in Fig. 8(b). As it follows, for Pt-doped Ni-Mn-Ga ($0.1 \leqslant x \leqslant 0.3$) the thermal hysteresis appears to be even smaller than for the stoichiometric composition Ni_2MnGa ($x = 0$). A narrow thermal hysteresis indicates the thermoelastic nature of the martensite transformation and that the interface between the parent and the martensite is mobile, as it would be expected for a martensite transformation exhibiting the shape memory effect [42,53].

C. Compositional variation of the saturation magnetization

The compositional dependent saturation magnetization $M(x)$ for $Ni_{2-x}Pt_xMnGa$ was obtained from the isothermal magnetization measurements at 2 K (Fig. 9). The corresponding $M_S(x)$ values are given in the inset. For the stoichiometric composition (Ni_2MnGa), $M_S(x) \approx 4.17\mu_B/f.u.$ This is in good agreement with earlier studies [21,59,60]. By increasing x, $M_S(x)$ is initially higher than the stoichiometric compound for compositions up to $x = 0.25$. This is consistent with the *ab initio* calculations, which show the increase of the Mn and Pt local moments within the ferromagnetic ground state [27]. However, upon further increase of Pt content ($x = 0.3, 0.4, 0.5,$ and 1), the $M_S(x)$ substantially drops down to $\approx 2.2\mu_B/f.u.$ for $x = 1$ (NiPtMnGa). Although, for $x = 1$ even at 7 T, the magnetization is not fully saturated, we have taken the value of $M_S(x)$ at 7 T as saturation moment for comparison. To study the origin of this reduction, we performed the neutron diffraction measurements as well as the *ab initio* calculations discussed in the following sections.

D. Evidence for the antisite disorder in NiPtMnGa ($x = 1$) from powder neutron diffraction

The magnetism of Mn-based Heusler alloys is mainly governed by Mn, which has been observed experimentally and shown by *ab initio* calculations for these systems.

FIG. 8. Structural and magnetic phase diagram (a) and phase transformation hysteresis (b) for $Ni_{2-x}Pt_xMnGa$($0 \leqslant x \leqslant 1$). PM_A, PM_M, FM_A, FM_M, and FI_M represents paramagnetic austenite, paramagnetic martensite, ferromagnetic austenite, ferromagnetic martensite, and ferrimagnetic martensite, respectively.
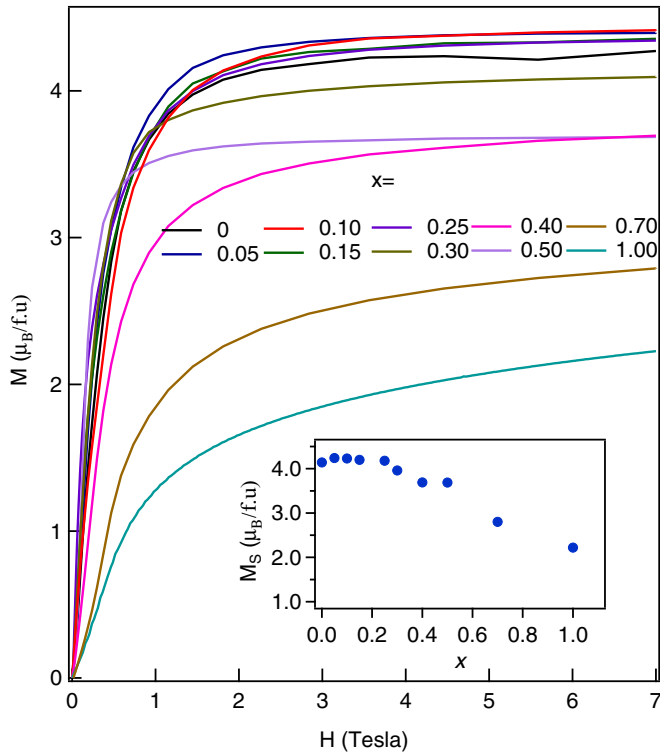
FIG. 9. Isothermal magnetization curves for $Ni_{2-x}Pt_xMnGa$ ($0 \leqslant x \leqslant 1$). The inset shows the variation of the saturation magnetization (taken at 7 T) with composition x.
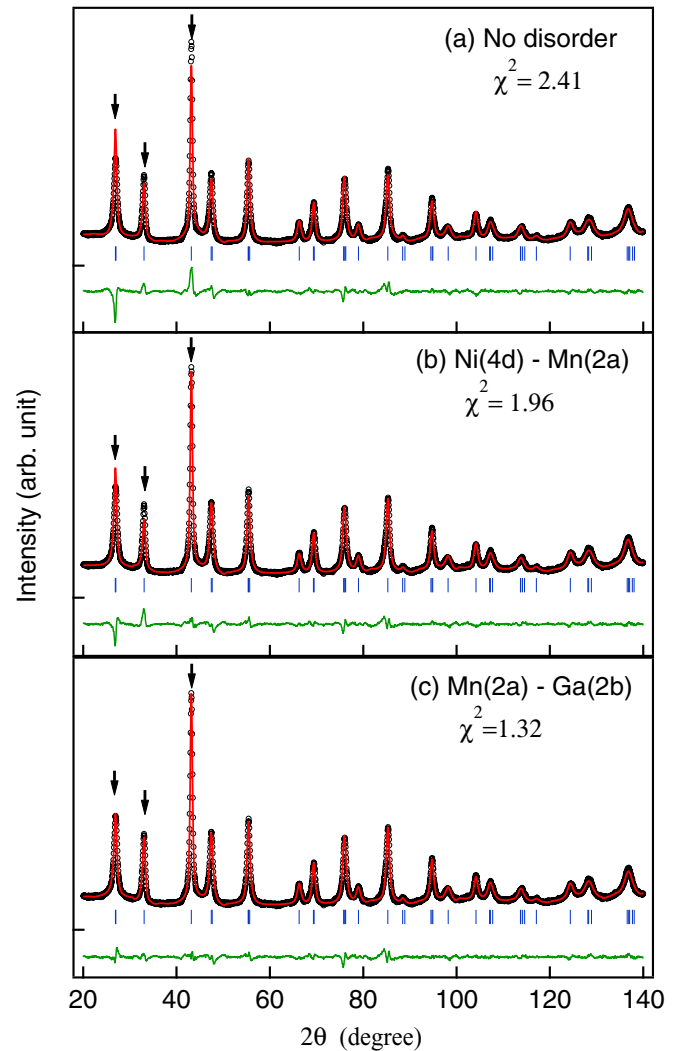

FIG. 10. Rietveld refinements of powder neutron diffraction pattern of NiPtMnGa at RT. The observed patterns (black circles) have been fitted (red solid lines) assuming (a) no disorder, (b) Ni($4d$)/Mn($2a$) disorder, and (c) Mn($2a$)/Ga($2b$) antisite disorder. The vertical arrows indicate the (101), (110), and (112) Bragg peaks (from left to right, respectively) of the tetragonal unit cell (SG $I4/mmm$). The green curve shows the difference between the measured and refined patterns. The vertical ticks are the Bragg peak positions.

However, the magnetization may change dramatically due to disorder [61–63]. Therefore, to study the origin of the large magnetization drop in NiPtMnGa, we performed neutron diffraction measurements and analyzed the data using the Rietveld refinement procedure (Fig. 10). In the first step of the refinement, we follow the LeBail fitting procedure using the tetragonal unit cell with SG $I4/mmm$. This model could index all the Bragg reflections confirming that NiPtMnGa exhibits the tetragonal structure at RT, which agrees with the XRD result [Fig. 5(d)]. In the next step, we performed the Rietveld refinement, by taking into account the atomic positions and occupancies of the atoms within the unit cell. The initial atomic positions were taken as Ni($4d$) and Pt($4d$), Mn($2a$), and Ga($2b$) [Fig. 11(a)]. Here, $4d$, $2a$, and $2b$ are the Wyckoff positions in the tetragonal unit cell. The nuclear scattering amplitudes for Ni, Mn, and Ga (10.3, -3.73, and

7.23 fm, respectively) are very distinct, which allows the determination of the actual atomic occupancies and the antisite disorder present in NiPtMnGa. Both fits, without and with Ni($4d$)/Mn($2a$) disorder are unsatisfactory [$\chi^2 = 2.41$, 1.96, respectively, see Figs. 10(a) and 10(b)]. However, if the antisite Mn($2a$)/Ga($2b$) disorder is taken into account, we obtain a much better fit [$\chi^2 = 1.32$, see Fig. 10(c)]. The tetragonal unit cell with Mn($2a$)/Ga($2b$) antisite defect is shown in Fig. 11(b).

The refined site occupancies listed in Table III reveal about 17% of the Mn($2a$)/Ga($2b$) antisite disorder. This may play an important role for the large decrease of magnetization, which is evidenced by the *ab initio* calculations discussed in the following section.

TABLE III. Parameters obtained from the Rietveld refinement of the neutron diffraction pattern for NiPtMnGa at RT.

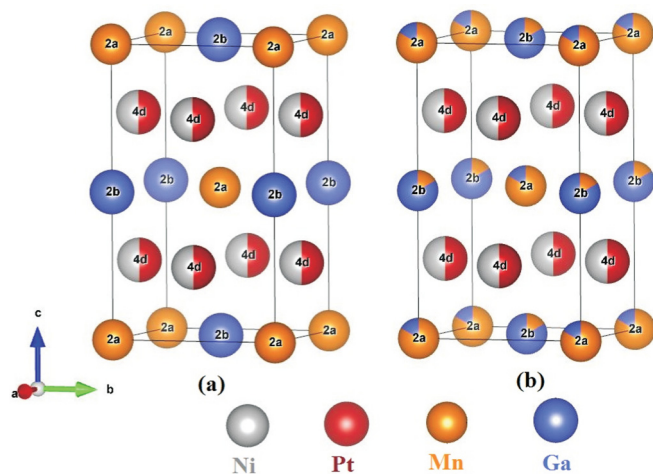| SG	$I4/mmm$		
Lattice parameters	$a = b = 3.964$ Å,	$c = 6.826$ Å	
Wyckoff site	$4d$	$2a$	$2b$
Pt occupancy	0.5	0	0
Ni occupancy	0.5	0	0
Mn occupancy	0	0.873(2)	0.163(2)
Ga occupancy	0	0.163(2)	0.873(2)

FIG. 11. Tetragonal unit cell (SG $I4/mmm$) of NiPtMnGa with (a) no antisite disorder and (b) Mn($2a$)-Ga($2b$) antisite disorder. 2a, 2b, and 4d represent the crystallographic Wyckoff positions within the tetragonal unit cell.

E. *Ab initio* calculations of the composition-dependent saturation magnetization

To explore the origin of the magnetization behavior in Ni-Pt-Mn-Ga compounds, we have theoretically studied the influence of structural (antisite) disorder on the total magnetic moments of $Ni_{2-x}Pt_xMnGa$ ($0 \leqslant x \leqslant 1$) as a function of Pt concentration (Fig. 12). Our earlier theoretical studies on manganese based magnetic Heusler alloys [64–66] carried out in the atomic sphere approximation method have shown that the magnitude of total and atomic magnetic moments are in reasonably good agreement with the corresponding experimental values. Henceforth, in the present calculations, the self-consistent potential has been calculated in the atomic sphere approximation. In order to emphasize the significance of antisite disorder in the explanation of the unusual concentration dependence of experimental $M_S(x)$

TABLE IV. Calculated partial magnetic moments (μ_B) of each atomic site in $Ni_{2-x}Pt_xMnGa$ ($0 \leqslant x \leqslant 1$) together with the total moments (μ_B/f.u) for the ordered (O) and antisite-disordered (AD) structures.

| Composition	Structure	Magnetic moments				
	SG $I4/mmm$	Mn($2b$)	Mn($2a$)	Ni($4d$)	Pt($4d$)	Total
$x = 0.0$	O	–	3.437	0.347	–	4.069
$x = 0.05$	O	–	3.447	0.349	0.169	4.076
$x = 0.10$	O	–	3.458	0.351	0.169	4.084
$x = 0.15$	O	–	3.469	0.353	0.170	4.090
$x = 0.20$	O	–	3.480	0.356	0.171	4.098
$x = 0.25$	O	–	3.491	0.358	0.171	4.105
$x = 0.3$	AD (3%)	−3.589	3.494	0.372	0.166	3.949
$x = 0.4$	AD (8%)	−3.567	3.517	0.389	0.164	3.632
$x = 0.5$	AD (8%)	−3.532	3.497	0.394	0.169	3.606
$x = 0.7$	AD (15%)	−3.549	3.534	0.338	0.136	2.976
$x = 1.0$	AD (17%)	−3.517	3.529	0.324	0.130	2.761
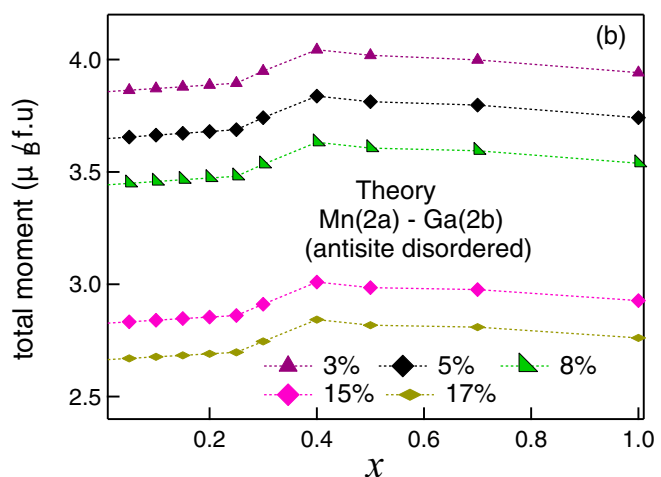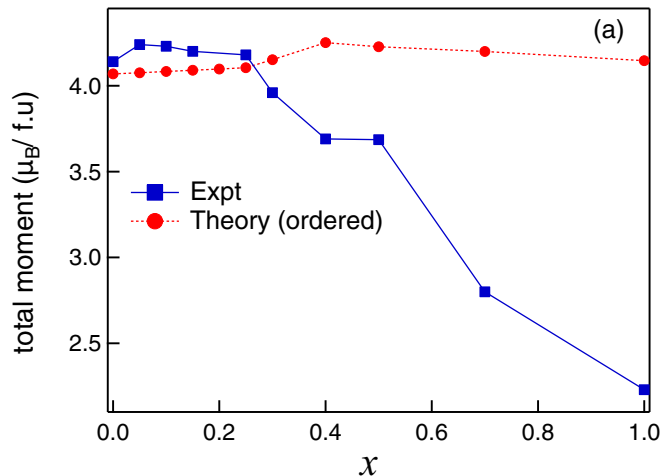
FIG. 12. The variation of magnetization in $Ni_{2-x}Pt_xMnGa$ ($0 \leqslant x \leqslant 1$) as a function of increasing Pt concentration x. (a) Experimental magnetization data (blue filled squares) and theoretically calculated total magnetic moments (red filled circles) in the ordered structure [Fig. 11(a)]. (b) Calculated total magnetic moments in the Mn($2a$)-Ga($2b$) antisite disordered structure [Fig. 11(b)] by varying the amount of antisite disorder.

[Fig. 12(a), blue filled squares], we have compared the calculated magnetic moments (red filled circles, labeled as "ordered") in the absence of antisite disorder with the experimental data. It can be clearly noticed from the Fig. 12(a) that within the composition range $0 \leqslant x \leqslant 0.25$, the calculated values of the magnetic moments exhibit a marginal increase from $4.07 \mu_B$/f.u. at $x = 0$ (Ni_2MnGa) to $4.11 \mu_B$/f.u. at $x = 0.25$ ($Ni_{1.75}Pt_{0.25}MnGa$), that agrees qualitatively with the experimental $M_S(x)$ as well as with earlier calculations [22,27,67]. The computed atomic magnetic moments (for Mn, Ni, and Pt atoms) in $Ni_{2-x}Pt_xMnGa$ listed in Table IV clearly shows that the magnetization is mainly confined to Mn($2a$) atoms indicating the localized character of the magnetization as observed for the Mn based Heusler alloys in agreement with previous theoretical studies [68–71]. In the composition range $0 \leqslant x \leqslant 0.25$, the narrow increase in $M_S(x)$ is mostly related to the linear variation of the moments on Mn($2a$) and Pt($4d$) atoms in comparison with the moments on Ni($4d$) atoms (Table IV). This indicates that the substitution of Pt

in $Ni_{2-x}Pt_xMnGa$ $0 \leqslant x \leqslant 0.25$ does not alter the nature of magnetic coupling between the Ni and Mn atoms resulting in a ferromagnetic state.

The experimental $M_S(x)$ in the composition range $0.25 \leqslant x \leqslant 1$ exhibits an unusual behavior resulting in an unexpected drop in $M_S(x)$ from $4.11\mu_B/f.u.$ at $x = 0.25$ to 2.2 $\mu_B/f.u.$ at $x = 1.0$ [Fig. 12(a), blue filled squares]. A cursory look at Fig. 12(a) reveals that the total magnetic moments calculated in the ordered structure, i.e., in the absence of antisite disorder demonstrates a contrasting behavior in comparison with the experimental $M_S(x)$ for $x > 0.25$. Therefore, in order to understand the drop in the experimental $M_S(x)$ curve, we have studied the effect of antisite disorder on the variation of the magnetic moments in Ni-Pt-Mn-Ga alloy for different percentage of Mn(2a)–Ga(2b) antisite disorder starting from 0% [Fig. 12(a)] up to 17% [Fig. 12(b)] as determined from the neutron diffraction analysis in NiPtMnGa (Fig. 10, and Table III). As illustrated in Fig. 12(b), we notice that the inclusion of Mn(2a)–Ga(2b) antisite disorder leads to a overall reduction of the magnitude of total magnetic moments in comparison with the ordered [0%, Fig. 12(a)] case. For example, the calculated magnetic moment for the composition $Ni_{1.7}Pt_{0.3}MnGa$ $(x = 0.3)$ in the ordered [Fig. 12(a)] and 3% antisite disordered [Fig. 12(b)] case is 4.15 $\mu_B/f.u.$ and 3.95 $\mu_B/f.u.$, respectively. Such a decrease in the total magnetic moments between the ordered and antisite disordered case can be attributed to the existence of an antiparallel coupling between the spins of the nearest neighbor Mn atoms located at the 2a and 2b Wyckoff sites [Fig. 11(b)]. This is in good agreement with the earlier study reported that the Mn atoms at Ga site coupled antiferromagnetically to the original Mn atoms at Mn site [72–74]. The antiparallel coupling between the nearest neighbor Mn atoms is clearly evident from the atomic magnetic moments shown in the Table IV for composition $x = 0.3$. Moreover, the experimental value of saturation magnetization for $x = 0.3$ is found to be 3.96 $\mu_B/f.u.$, which is in very good agreement with the computed value 3.95 $\mu_B/f.u.$ obtained while 3% Mn(2a)–Ga(2b) antisite disorder was taken into account. Henceforth, in Fig. 13, we have shown 3% antisite disorder for $x = 0.3$ indicating the optimum amount of antisite disorder that would be sufficient to describe the magnetization in $Ni_{1.7}Pt_{0.3}MnGa$ $(x = 0.3)$. On similar lines we have estimated the most probable amounts of antisite disorder in the composition range $0.4 \leqslant x \leqslant 1$, which are mentioned in the Fig. 13 as well as given in the Table IV. We find that the unusual behavior of the experimental magnetization (Fig. 13) of $Ni_{2-x}Pt_xMnGa$ $(0 \leqslant x \leqslant 1)$ arises due to the presence of different magnetic phases like ferromagnetic and ferrimagnetic phase corresponding to the composition range $0 \leqslant x \leqslant 0.25$ and $0.3 \leqslant x \leqslant 1$, respectively, triggered by the presences of Mn(2a)–Ga(2b) antisite disorder. Although, theory suggests the onset of ferrimagnetism at $x = 0.3$, the experimental signature of this phenomenon is evident at $x = 0.7$ [Fig. 7(i)]. We anticipate that this difference might be arising because a minimum amount of Mn(2a)–Ga(2b) antisite disorder [for example 15%, $(x = 0.7)$] might have to exist in the Ni-Pt-Mn-Ga alloy for the considerable dominance of the nearest-neighbor antiferromagnetic coupling between the
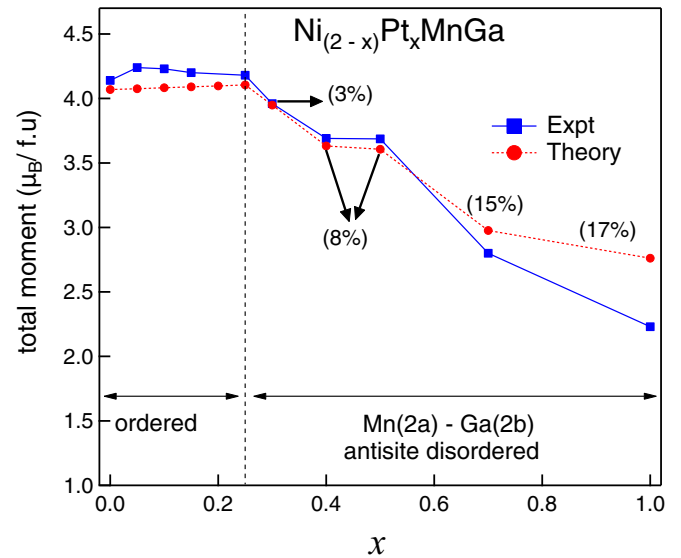

FIG. 13. The dependency of the saturated magnetization in $Ni_{2-x}Pt_xMnGa$ $(0 \leqslant x \leqslant 1)$ as a function of increasing Pt concentration x. Red filled circles correspond to theoretical data. The experimental data of saturation magnetization measured at 2 K are also plotted (blue filled squares). The solid lines serves as a guide to the eye.

Mn atoms resulting in the stabilization of the ferrimagnetic phase.

IV. SUMMARY AND CONCLUSIONS

We have studied the effect of Pt substitution on the structural and magnetic properties of $Ni_{2-x}Pt_xMnGa$ $(0 \leqslant x \leqslant 1)$ ferromagnetic shape memory alloys by x-ray diffraction, magnetization, neutron diffraction measurements and *ab initio* calculations. The RT XRD shows that in the composition range $0 \leqslant x \leqslant 0.25$ the cubic austenite phase is stable, while the $x = 0.3$ compositions shows the monoclinic modulated martensite phase with seven-layer periodicity of modulation. We have determined the space group and atomic positions of the 7M-modulated monoclinic structure. Compositions with higher Pt content $(x \geqslant 0.4)$ exhibit stable nonmodulated tetragonal structure in the martensite phase. By replacing Ni with Pt, the martensite transition temperature increases, which is in good agreement with earlier theoretical results [22].

On the other hand, the magnetic transition temperature decreases with increasing Pt content. The $x = 0.7$ and 1 compositions show a magnetic transition from PM to FI within the martensite phase. A minimum thermal hysteresis of transformation (1.5 K) is observed for $x = 0.25$. To the best of our knowledge, this is the smallest value ever reported for these type of alloys. Since thermal hysteresis plays a major role in the reversibility of the phase transition, our results indicate the importance of these alloys in practical applications.

The saturation magnetization as a function of Pt content shows a nontrivial behavior: it increases for $x \leqslant 0.25$ and decreases for $x \geqslant 0.3$. The magnetic moments in Ni_2MnGa mainly reside on Mn atoms $(\approx 4\mu_B)$, while Ni has a small

moment ($\approx 0.3\mu_B$). Therefore, by replacing Ni with Pt, the saturation magnetization is not expected to change drastically. This is in contradiction with a large magnetization drop observed for the $x = 0.7$ and 1 (NiPtMnGa) compositions. The Rietveld analysis of the neutron diffraction data reveals the presence of Mn/Ga antisite disorder, where $\approx 17\%$ of Mn occupies the original Ga sites. The *ab initio* calculations accounting for antisite disorder reveal an antiparallel alignment of the Mn($2b$) (Mn on the original Ga sites) with respect to Mn($2a$) that is responsible for the reduction of the magnetization in NiPtMnGa and other Pt-substituted Ni$_2$MnGa FSMAs.

[1] K. Ullakko, J. K. Huang, C. Kantner, R. C. O'Handley, and V. V. Kokorin, Appl. Phys. Lett. **69**, 1966 (1996).

[2] S. J. Murray, M. Marioni, S. M. Allen, R. C. O'Handley, and T. A. Lograsso, Appl. Phys. Lett. **77**, 886 (2000).

[3] A. Sozinov, A. A. Likhachev, N. Lanska, and K. Ullakko, Appl. Phys. Lett. **80**, 1746 (2002).

[4] K. Bhattacharya, *Microstructure of Martensite* (Oxford University Press, Oxford, 2003).

[5] P. J. Webster, K. R. A. Ziebeck, S. L. Town, and M. S. Peak, Philos. Mag. B **49**, 295 (1984).

[6] C. Biswas, R. Rawat, and S. R. Barman, Appl. Phys. Lett. **86**, 202508 (2005).

[7] S. Banik, S. Singh, R. Rawat, P. K. Mukhopadhyay, B. L. Ahuja, A. M. Awasthi, S. R. Barman, and E. V. Sampathkumaran, J. Appl. Phys. **106**, 103919 (2009).

[8] S. Singh, R. Rawat, and S. R. Barman, Appl. Phys. Lett. **99**, 021902 (2011).

[9] J. Marcos, L. Mañosa, A. Planes, F. Casanova, X. Batlle, and A. Labarta, Phys. Rev. B **68**, 094401 (2003).

[10] F. X. Hu, B. Shen, and J. Sun, Appl. Phys. Lett. **76**, 3460 (2000).

[11] F.-x. Hu, B.-g. Shen, J.-r. Sun, and G.-h. Wu, Phys. Rev. B **64**, 132412 (2001).

[12] S. Singh, J. Nayak, A. Rai, P. Rajput, A. H. Hill, S. R. Barman, and D. Pandey, J. Phys.: Condens. Matter **25**, 212203 (2013); S. Singh, S. R. Barman, and D. Pandey, Z. Kristallogr. **230**, 13 (2015).

[13] S. W. D'Souza, A. Rai, J. Nayak, M. Maniraj, R. S. Dhaka, S. R. Barman, D. L. Schlagel, T. A. Lograsso, and A. Chakrabarti, Phys. Rev. B **85**, 085123 (2012).

[14] J. Pons, E. Cesari, C. Seguí, F. Masdeu, and R. Santamarta, Mater. Sci. Eng., A **481**, 57 (2008).

[15] S. R. Barman, A. Chakrabarti, Sanjay Singh, S. Banik, S. Bhardwaj, P. L. Paulose, B. A. Chalke, A. K. Panda, A. Mitra, and A. M. Awasthi, Phys. Rev. B **78**, 134406 (2008).

[16] A. Fujita, K. Fukamichi, F. Gejima, R. Kainuma, and K. Ishida, Appl. Phys. Lett. **77**, 3054 (2000).

[17] H. B. Wang, F. Chen, Z. Y. Gao, W. Cai, and L. C. Zhao, Mater. Sci. Eng. A **438**, 990 (2006)

[18] K. Koho, O. Söderberg, N. Lanska, Y. Ge, X. Liu, L. Straka, J. Vimpari, O. Heczko, and V. K. Lindroos, Mater. Sci. Eng. A **378**, 384 (2004).

[19] H. Morito, K. Oikawa, A. Fujita, K. Fukamichi, R. Kainuma, and K. Ishida, Scr. Mater. **53**, 1237 (2005).

[20] M. Kataoka, K. Endo, N. Kudo, T. Kanomata, H. Nishihara, T. Shishido, R. Y. Umetsu, M. Nagasako, and R. Kainuma, Phys. Rev. B **82**, 214423 (2010).

[21] T. Kanomata, S. Nunoki, K. Endo, M. Kataoka, H. Nishihara, V. V. Khovaylo, R. Y. Umetsu, T. Shishido, M. Nagasako, R. Kainuma, and K. R. A. Ziebeck, Phys. Rev. B **85**, 134421 (2012).

[22] M. Siewert, M. E. Gruner, A. Dannenberg, A. Chakrabarti, H. C. Herper, M. Wuttig, S. R. Barman, S. Singh, A. Al-Zubi, T. Hickel, J. Neugebauer, M. Gillessen, R. Dronskowski, and P. Entel, Appl. Phys. Lett. **99**, 191904 (2011).

[23] P. Entel, M. Siewert, M. E. Gruner, A. Chakrabarti, S. R. Barman, V. V. Sokolovskiy, and V. D. Buchelnikov, J. Alloys Compd. **577**, S107 (2013).

[24] B. Dutta, T. Hickel, P. Entel, and J. Neugebauer, J. Phase Equilib. Diffus. **35**, 695 (2014).

[25] Y. Kishi, Z. Yajima, K. Shimizu, and M. Wuttig, Mater. Sci. Eng. A **378**, 361 (2004).

[26] S. Singh, K. R. A. Ziebeck, E. Suard, P. Rajput, S. Bhardwaj, A. M. Awasthi, and S. R. Barman, Appl. Phys. Lett. **101**, 171904 (2012).

[27] S. Singh, S. W. D'Souza, K. Mukherjee, P. Kushwaha, S. R. Barman, S. Agarwal, P. K. Mukhopadhyay, A. Chakrabarti, and E. V. Sampathkumaran, Appl. Phys. Lett. **104**, 231909 (2014).

[28] V. Petricek, M. Dusek, and L. Palatinus, JANA2000: *The Crystallographic Computing System* (Institute of Physics, Prague, Czech Republic, 2000); J. R. Carvajal, FULLPROF, a Rietveld refinement and pattern matching analysis program, Laboratoire Leon Brillouin, CEA-CNRS, France (2000).

[29] H. Ebert, D. Ködderitzsch, and J. Minár, Rep. Prog. Phys. **74**, 096501 (2011).

[30] P. Soven, Phys. Rev. **156**, 809 (1967).

[31] B. L. Gyorffy, Phys. Rev. B **5**, 2382 (1972).

[32] S. H. Vosko, L. Wilk, and M. Nusair, Can. J. Phys. **58**, 1200 (1980).

[33] V. A. Chernenko, E. Cesari, V. V. Kokorin, and I. N. Vitenko, Scr. Metall. Mater. **33**, 1239 (1995).

[34] J. Pons, V. A. Chernenko, R. Santamarta, and E. Cesari, Acta Mater. **48**, 3027 (2000).

[35] N. Lanska, O. Söderberg, A. Sozinov, Y. Ge, K. Ullakko, and V. K. Lindroos, J. Appl. Phys. **95**, 8074 (2004).

[36] V. A. Chernenko, C. Segui, E. Cesari, J. Pons, and V. V. Kokorin, Phys. Rev. B **57**, 2659 (1998).

[37] O. Heczko, N. Lanska, O. Soderberg, and K. Ullakko, J. Magn. Magn. Mater. **242-245**, 1446 (2002).

[38] A. Ayuela, J. Enkovaara, K. Ullakko, and R. M. Nieminen, J. Phys.: Condens. Matter **11**, 2017 (1999).

[39] V. V. Godlevsky and K. M. Rabe, Phys. Rev. B **63**, 134407 (2001).

[40] A. Ayuela, J. Enkovaara, and R. M. Nieminen, J. Phys.: Condens. Matter **14**, 5325 (2002).

[41] C. Bungaro, K. M. Rabe, and A. Dal Corso, Phys. Rev. B **68**, 134104 (2003).

[42] S. Banik, R. Ranjan, A. Chakrabarti, S. Bhardwaj, N. P. Lalla, A. M. Awasthi, V. Sathe, D. M. Phase, P. K. Mukhopadhyay, D. Pandey, and S. R. Barman, Phys. Rev. B **75**, 104107 (2007).

[43] R. Ranjan, S. Banik, S. R. Barman, U. Kumar, P. K. Mukhopadhyay, and D. Pandey, Phys. Rev. B **74**, 224443 (2006).

[44] B. Wedel, M. Suzuki, Y. Murakami, C. Wedel, T. Suzuki, D. Shindo, and K. Itagaki, J. Alloys Compd. **290**, 137 (1999).

[45] P. J. Brown, J. Crangle, T. Kanomata, M. Matsumoto, K.-U. Neumann, B. Ouladdiaf, and K. R. A. Ziebeck, J. Phys.: Condens. Matter **14**, 10159 (2002).

[46] L. Righi, F. Albertini, G. Calestani, L. Pareti, A. Paoluzi, C. Ritter, P. A. Algarabel, L. Morellon, and M. R. Ibarra, J. Solid State Chem. **179**, 3525 (2006).

[47] T. Krenke, E. Duman, M. Acet, E. F. Wassermann, X. Moya, L. Mañosa, A. Planes, E. Suard, and B. Ouladdiaf, Phys. Rev. B **75**, 104414 (2007).

[48] S. Singh, V. Petricek, P. Rajput, A. H. Hill, E. Suard, S. R. Barman, and D. Pandey, Phys. Rev. B **90**, 014109 (2014).

[49] L. Righi, F. Albertini, E. Villa, A. Paoluzi, G. Calestani, V. Chernenko, S. Besseghini, C. Ritter, and F. Passaretti, Acta Mater. **56**, 4529 (2008).

[50] S. Singh, M. Maniraj, S. W. D'Souza, R. Ranjan, and S. R. Barman, Appl. Phys. Lett. **96**, 081904 (2010).

[51] A. Sozinov, N. Lanska, A. Soroka, and W. Zou, Appl. Phys. Lett. **102**, 021902 (2013).

[52] M. Zelený, A. Sozinov, L. Straka, T. Björkman, and R. M. Nieminen, Phys. Rev. B **89**, 184103 (2014).

[53] S. Banik, A. Chakrabarti, U. Kumar, P. K. Mukhopadhyay, A. M. Awasthi, R. Ranjan, J. Schneider, B. L. Ahuja, and S. R. Barman, Phys. Rev. B **74**, 085110 (2006).

[54] A. N. Vasil'ev, A. D. Bozhko, V. V. Khovailo, I. E. Dikshtein, V. G. Shavrov, V. D. Buchelnikov, M. Matsumoto, S. Suzuki, T. Takagi, and J. Tani, Phys. Rev. B **59**, 1113 (1999).

[55] R. Ranjan, S. Singh, H. Boysen, D. Trots, S. Banik, A. M. Awasthi, P. K. Mukhopadhyay, and S. R. Barman, J. Appl. Phys. **106**, 033510 (2009).

[56] B. L. Ahuja, A. Dashora, N. L. Heda, K. R. Priolkar, L. Vadkhiya, M. Itou, N. Lobo, Y. Sakurai, A. Chakrabarti, S. Singh, and S. R. Barman, J. Phys.: Condens. Matter **22**, 446001 (2010).

[57] S. Singh, P. Kushwaha, F. Scheibel, Hanns-Peter Liermann, S. R. Barman, M. Acet, C. Felser, and Dhananjai Pandey, Phys. Rev. B **92**, 020105(R) (2015).

[58] A. K. Nayak, M. Nicklas, S. Chadov, C. Shekhar, Y. Skourski, J. Winterlik, and C. Felser, Phys. Rev. Lett. **110**, 127204 (2013).

[59] B. L. Ahuja, B. K. Sharma, S. Mathur, N. L. Heda, M. Itou, A. Andrejczuk, Y. Sakurai, A. Chakrabarti, S. Banik, A. M. Awasthi, and S. R. Barman, Phys. Rev. B **75**, 134403 (2007).

[60] V. V. Khovailo, V. Novosad, T. Takagi, D. A. Filippov, R. Z. Levitin, and A. N. Vasilev, Phys. Rev. B **70**, 174413 (2004).

[61] M. Acet, E. Duman, E. F. Wassermann, L. Mañosa, and A. Planes, J. Appl. Phys. **92**, 3867 (2002).

[62] T. Kanomata, M. Kikuchi, and H. Yamauchi, J. Alloys Comp. **414**, 1 (2006).

[63] S. Khmelevskyi, E. Simon, and L. Szunyogh, Phys. Rev. B **91**, 094432 (2015).

[64] S. Singh, R. Rawat, S. E. Muthu, S. W. D'Souza, E. Suard, A. Senyshyn, S. Banik, P. Rajput, S. Bhardwaj, A. M. Awasthi, R. Ranjan, S. Arumugam, D. L. Schlagel, T. A. Lograsso, A. Chakrabarti, and S. R. Barman, Phys. Rev. Lett. **109**, 246601 (2012).

[65] A. K. Nayak, C. S. Mejia, S. W. DSouza, S. Chadov, Y. Skourski, C. Felser, and M. Nicklas, Phys. Rev. B **90**, 220408(R) (2014).

[66] S. Singh, L. Caron, S. W. D'Souza, T. Fichtner, G. Porcari, S. Fabbrici, C. Shekhar, S. Chadov, M. Solzi, and C. Felser, Adv. Mater., doi:10.1002/adma.201505571.

[67] S. W. D'Souza, T. Roy, S. R. Barman, and A. Chakrabarti, J. Phys.: Condens. Matter **26**, 506001 (2014).

[68] E. Şaşioğlu, L. M. Sandratskii, and P. Bruno, Phys. Rev. B **70**, 024427 (2004).

[69] A. Deb and Y. Sakurai, J. Phys.: Condens. Matter **12**, 2997 (2000).

[70] J. Kübler, A. R. Williams, and C. B. Sommers, Phys. Rev. B **28**, 1745 (1983).

[71] G. E. Bacon and J. S. Plant, J. Phys. F **3**, 2003 (1973).

[72] J. Enkovaara, O. Heczko, A. Ayuela, and R. M. Nieminen, Phys. Rev. B **67**, 212405 (2003).

[73] M. L. Richard, J. Feuchtwanger, S. M. Allen, R. C. OHandley, P. Lázpita, J. M. Barandiarán, J. Gutiérrez, B. Ouladdiaf, C. Mondelli, T. A. Lograsso, and D. L. Schlagel, Philos. Mag. **87**, 3437 (2007).

[74] P. Lázpita, J. M. Barandiarán, J. Gutiérrez, J. Feuchtwanger, V. A. Chernenko, and M. L. Richard, New J. Phys. **13**, 033039 (2011).